Batteries & Supercaps

Articles
doi.org/10.1002/batt.202100157

Chemistry
Europe
European Chemical
Societies Publishing

Oxygen Vacancies Enhance Lithium-Ion Storage Properties of TiO₂ Hierarchical Spheres

Zhaoqian Li,[a] Yuqi Peng,[a] Xianxi Zhang,[b] Yingke Ren,[e] Wangchao Chen,[f] Feng Xu,[g] Ning Wang,[g] Chaofeng Liu,[d] Lie Mo,[a] Yanwei Ding,[h] Linhua Hu,*[a] Denghui Ji,*[c] and Guozhong Cao*[d]

Titanium dioxide (TiO₂) is a promising electrode material for reversible lithium storage. However, the poor electronic conductivity, sluggish diffusivity, and intrinsic kinetics limit hinder its fast lithium storage capability. Here we present that the oxygen-deficient TiO₂ hierarchical spheres can address the issues for high capacity, long-term lithium-ion battery anode. First-principles calculations show that introducing oxygen vacancies to anatase TiO₂ can reduce the bandgap, thus improving the electronic conductivity and further the lithium storage properties of TiO₂. By annealing TiO₂/H₂Ti₅O₁₁·3H₂O hierarchical spheres precursor in nitrogen, accompanying with the phase transfer process, the growth of TiO₂ crystallites is restricted due to the generation of residual carbon species, resulting in a well maintained hierarchical spherical structure. Rich oxygen vacancies are generated in the oxygen-deficient environment and evidenced by EPR, XPS, and UV-Vis spectra, which enable the TiO₂ hierarchical spheres reduced bandgap. The oxygen vacancies in the as-obtained TiO₂ hierarchical spheres together with the high structural integrity of the hierarchical spheres gives rise to superior lithium storage properties including a high specific capacity of 282 mAh g⁻¹ at 200 mA g⁻¹, and long-term cycling stability with a capacity retention of 85.2 % at 4 A g⁻¹ over 10000 cycles.

1. Introduction

Lithium-ion batteries (LIBs) have achieved tremendous advances as an efficient energy storage and supply approach for portable electronics and electric vehicles.[1] Presently, one of the urgent tasks is searching for suitable lithium host materials to meet the ever-growing needs of batteries with high energy and power densities. Anatase TiO₂ is a promising host material for high-performance LIBs due to its unique features including cost-effectiveness, chemical stability, and environmental benignity.[2] During its charging/discharging process, the reversible Li⁺ ions insertion, and extraction in the interstitial crystal vacancies leads to the formation of Li$_x$TiO₂.[3] The theoretical capacity of anatase TiO₂ is 167 mAh g⁻¹, corresponding to 0.5 lithium-ion inserted in TiO₂.[4] However, the low ionic and electrical conductivities seriously restricted its electrochemical performance, causing limited lithium storage capacity and poor cycling performance.[5] Therefore, increasing lithium-ion storage properties of anatase TiO₂ is a key task.

The creation of oxygen vacancies is an effective way to improve the ion diffusion problem.[6] The presence of oxygen vacancies in TiO₂ could act as shallow donors, narrowing bandgap (E_g), which has been demonstrated helpful for the improvement of electronic conductivity, producing superior ion

[a] Dr. Z. Li, Dr. Y. Peng, Dr. L. Mo, Prof. L. Hu
Key Laboratory of Photovoltaic and Energy Conservation Materials,
CAS, Institute of Solid State Physics,
Hefei Institutes of Physical Science
Chinese Academy of Sciences
Hefei, Anhui, 230031, China
E-mail: lhhu@rntek.cas.cn

[b] Prof. X. Zhang
Shandong Provincial Key Laboratory/Collaborative Innovation Center
of Chemical Energy Storage & Novel Cell Technology
School of Chemistry and Chemical Engineering
Liaocheng University
Liaocheng, 252000, China

[c] Dr. D. Ji
College of Physics, Mechanical and Electronical College
Shijiazhuang University
Shijiazhuang City, 050035, China
E-mail: jidenghui2007@163.com

[d] Dr. C. Liu, Prof. G. Cao
Department of Materials Science and Engineering
University of Washington
Seattle, WA 98195, USA
E-mail: gzcao@u.washington.edu

[e] Dr. Y. Ren
College of Science
Hebei University of Science and Technology
Shijiazhuang, 050018, China

[f] Dr. W. Chen
School of Chemistry and Chemical Engineering,
Anhui Province Key Laboratory of
Advanced Catalytic Materials and Reaction Engineering
Hefei University of Technology
Hefei, 230009, China

[g] Dr. F. Xu, N. Wang
High Magnetic Field Laboratory
Chinese Academy of Sciences
Hefei 230031, China

[h] Dr. Y. Ding
Hefei National Laboratory for Physical Sciences at the Microscale
University of Science and Technology of China
Hefei 230026, China

Supporting information for this article is available on the WWW under
https://doi.org/10.1002/batt.202100157

storage capabilities.[7] Designing nanostructured anatase TiO_2 materials is another promising strategy to improve lithium-ion storage capability and even exceed its theoretical limit. Due to the crystal size effect, anatase TiO_2 nanocrystals could store excess lithium because of the pseudocapacitive surface and interfacial storage mechanism.[8] Reducing TiO_2 particle size also facilitates contact with the electrolyte, leading to improved electron transport and Li^+ ion diffusion.[9] However, the high surface energy of nanoparticles causes aggregate during the charge-discharge process, leading to the loss of active sites, capacity fading, and short lifespan.[9] Recently, it has been validated that TiO_2 hierarchical structures composed of primary nanoparticles could partly tackle this problem. Besides, the porous hierarchical structure can provide plenty of Li-ion diffusion channels, giving rise to high electrochemical activity.[10] Therefore, The lithium storage capability of such an oxygen-deficient TiO_2 electrode composed of hierarchical structure and small primary nanoparticles should be an integration of the favorable features, including crystal-size-effect, robust structural stability, and enhanced charge diffusion kinetic.

Here we report a solvothermal method to synthesize nanosheets constructed $TiO_2/H_2Ti_5O_{11}\cdot3H_2O$ hierarchical spheres (TiO_2/HTO). By annealing the TiO_2/HTO precursor in the N_2 atmosphere, the growth of TiO_2 crystallites is efficiently restricted due to the generation of residual carbon species, resulting in a perfectly maintained hierarchical spherical structure of the high crystallinity anatase TiO_2. Accompanying with the phase transfer process, oxygen vacancies are generated in the oxygen-deficient environment, leading to narrowed bandgap and improved electrical conductivity of the TiO_2 hierarchical spheres. Owing to the synergistic combination of the small size, porous structure, oxygen vacancies, and high structural integrity, the as obtained oxygen-deficient TiO_2 hierarchical spheres is utilized as anode in LIBs and delivers a high specific capacity of 282 mAh g^{-1} at 200 mA g^{-1}, and a withstanding long-term cycling stability with a capacity retention of 85.2% at 4 A g^{-1} over 10000 cycles. The lithium ion storage performance is better than most reported oxygen-deficient TiO_2[11] and other TiO_2 materials (Table S1).[12]

2. Results and Discussion

Figure 1 shows the crystal structure models for pristine anatase TiO_2 and oxygen-deficient model $Ti_{16}O_{31}$ and calculated electronic density of states (EDOS) using the DFT+U method. The calculated band gap of the pristine TiO_2 is 3.204 eV, which agrees well with its experimental value. After introducing oxygen vacancy, the formation of oxygen vacancies provides extra electrons and can affect the electronic structure of TiO_2. Here, the oxygen-deficient model shows a reduced bandgap of 2.711 eV. The extra electrons and reduced bandgap will contribute to the improved electronic conductivity and charge carrier transport.[6b,13]

Figure 2(a) is the SEM image of the precursor which consists of uniform, hierarchical spheres with an average diameter of ca.
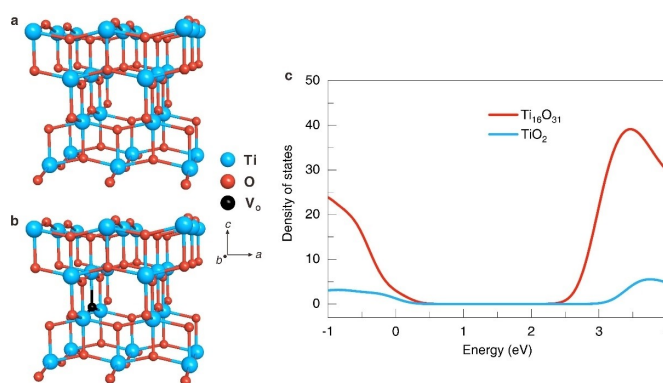

Figure 1. Crystal structure models for a) TiO_2 and b) $Ti_{16}O_{31}$. c) Calculated electronic density of states for TiO_2 and $Ti_{16}O_{31}$ using the DFT+U method.

900 nm. The magnified SEM [Figure 2(b)] and TEM images [Figure 2(c,d)] confirm that the sphere is entirely constituted of self-organized nanosheets from the edge to the center. HRTEM [Figure 2(e)] demonstrates that the nanosheet is composed of tiny nanoparticles. The large interlayer spacings of ca. 1.02 nm [Figure 2(e)] correspond to the distance between (200) planes of $H_2Ti_5O_{11}\cdot3H_2O$, (JCPDS No. 44-0130). The lattice interspacing of 0.35 nm shown by the HRTEM image [Figure 2(f)] can be assigned to the (101) planes of anatase TiO_2 (JCPDS No. 21-1272). The broad and weak peaks of the XRD pattern (Figure S1) evidences the nanosized nature of the primary particles. XRD pattern shows the coexistence of anatase TiO_2 and protonated titanate. The peaks located at around 8.5° and 27.1° can be assigned to the (200) and (310) facets of $H_2Ti_5O_{11}\cdot3H_2O$, (JCPDS No. 44-0130), while the other peaks can be indexed to anatase TiO_2. The peak at around 8.5° corresponding to a d spacing value of 10.4 Å coincides well with the HRTEM observation. TG-DSC analysis was conducted to confirm the molar ratio of the $H_2Ti_5O_{11}\cdot3H_2O$ in the precursor (Figure S2). The rapid weight loss of ~9 wt.% in the range 30–100 °C accompanying by a sharp endothermal peak I is due to the physically adsorbed water and 2 mol of free interlayer water/formula. From 100 to 250 °C, a gradual loss of 3.6 wt.% accompanying two endothermal peaks II and III corresponds to another 2 mol of free interlayer water/formula.[14] Upon 250 °C, the weight loss of ca. 10 wt.% mainly comes from the combustion of organic species accompanying the strong exothermal process IV. The existence of organic species was also confirmed by the FTIR spectrum (Figure S3), which might come from organic species, e.g., isopropyl alcohol and ethylenediamine, adsorbed onto the surface since the TiO_2/HTO precursor are synthesized in organic solvents, it is inevitable adsorbing organic molecules on the surface of nanocrystals. According to the weight loss percentage in the range 100–250 °C, the molar ratio of the $H_2Ti_5O_{11}wt\%3H_2O$ in the TiO_2/HTO precursor was calculated to be ca. 16 mol%.

To understand the formation mechanism of such nanosheet-based hierarchical spheres, different experimental conditions were investigated. First, time-dependent solvothermal experiments were performed to gain insights into the evolution process. Figure 3(a–d) depict the SEM images of the products
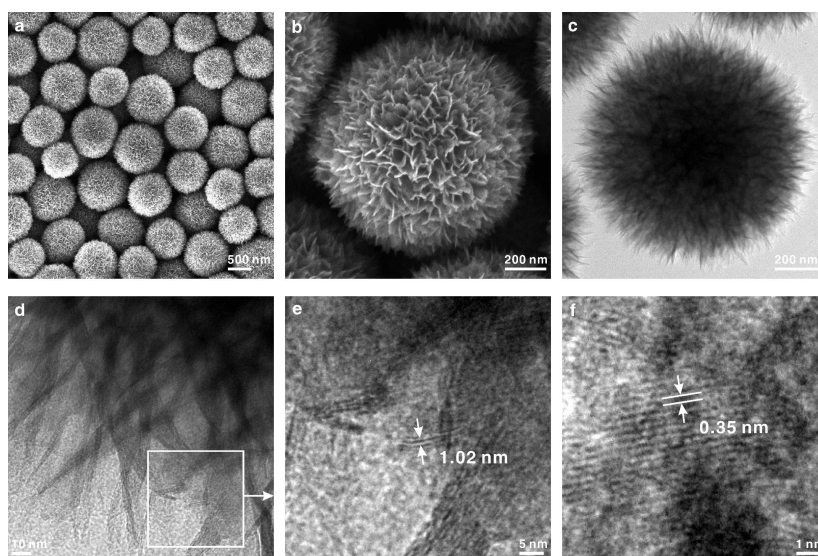
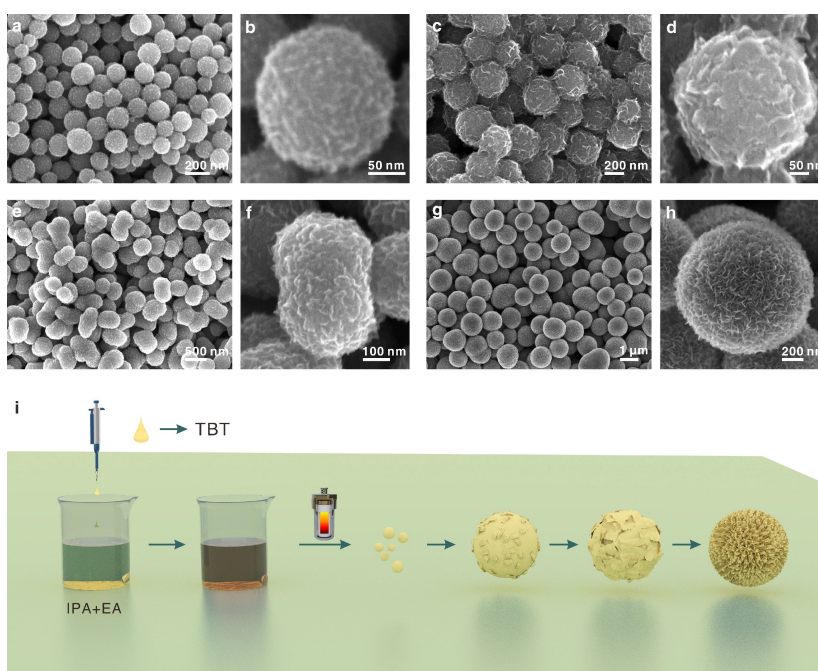**Figure 2.** a–c) SEM and d–f) TEM images of the TiO$_2$/HTO precursor.

Figure 3. a–d) SEM images of the samples prepared at 200 °C for different reaction time: a, b) 3 h. c, d) 6 h. e–h) SEM images of the samples prepared with different amounts of ethylenediamine: e, f) 0.05 mL. g, h) 0.2 mL. i) Schematic illustration of the formation process of the precursor. TBT, IPA, and EA represent tetra-n-butyl titanate, isopropyl alcohol, and ethylenediamine, respectively.

obtained at different stages of solvothermal reaction. Before the solvothermal reaction, the solution consisted of IPA, EA and TBT show a yellow transparent state. After solvothermal treatment, at the initial stage (3 h), the product is composed of solid spheres with a rough surface [Figure 3(a)]. Only small nanosheets grow on the surface of spheres (Figure 3b). With extending the reaction time to 6 h, large nanosheets appeared on the sphere surface [Figure 3(c,d)]. Eventually, after reaction for 12 h, the spheres evolved into the well-defined uniform TiO$_2$ hierarchical spheres entirely composed of ultrathin nano-

sheets (Figure 2). Accompanying with the morphology and structure evolution, the diameters of spheres at different reaction stages grow from ca. 200 nm, 400 nm to 900 nm. In addition to the reaction time, the amount of EA also has a dramatic influence on the morphology and structure of the products [Figure 3(e–h)]. Only irregular nanostructures with non-spherical morphology formed when 0.05 mL of EA was added, and the as-prepared products showed a sparse nanosheets distribution on the surface [Figure 3(e,f)]. Increasing the amount of EA to 0.2 mL, the final product shows a similar

hierarchical spherical structure with the TiO$_2$/HTO precursor (Figure 2) but possesses more densely nanosheets distribution and ununiform sphere size [Figure 3(g, h)].

Based on the above experimental observations, the formation of well-defined TiO$_2$/HTO hierarchical spheres could be explained by a coordination-crystallization-dissolution-recrystallization mechanism, which just like the Ostwald-ripening process.[15] Here, the existence of ethylenediamine (EA) plays a significant role in the formation of nanosheets and the uniformity of spheres. EA has a strong coordination function and can coordinate with many metal ions, resulting in stable composites.

The amino on EA prefers to coordinate with special crystal planes in the metal oxide nanomaterials formation process which often gives rise to nanosheets structure.[4b,16] As schematically depicted in Figure 3(i), prior to the solvothermal reaction, the transparency of the solution suggests no hydrolysis of TBT occurred. The solution stability stems from the coordination effect between EA and TBT. Under heating, the coordination state of the Ti source was destroyed. The hydrolysis of the Ti source occurs with the etherification of IPA,[17] leading to the formation of nanospheres due to the crystallization and assembly of TiO$_2$ nanocrystalline. In this stage, hydrolysis and crystallization govern the reaction, numerous TiO$_2$ nanocrystalline was produced but EA molecular cannot cover all nanocrystalline and generate nanosheets. Therefore, only sparse nanosheets appeared on the surface of spheres. With the reaction proceeded, some thermodynamically unstable nanocrystalline will dissolve and recrystallized to stable large crystalline. Because of the strong coordination

effect of EA molecular, the recrystallization process prefers to form nanosheet structures at the expense of gradual consumption of internal solid parts. After the completion of this reaction, the hierarchical spheres will be entirely constructed by nanosheets and exhibit a larger sphere size (Figure 2).

The TiO$_2$/HTO precursor can transform to high crystallinity anatase TiO$_2$ upon calcination. Previous studies show that the choice of heat-treated atmosphere is crucial to the final structure and properties of the product.[15a,18] After annealing the TiO$_2$/HTO precursor at 500 °C in N$_2$ and air, the B-THS and W-THS show narrow and sharp XRD peaks (Figures 4a and S4), revealing the good crystallinity. Distinct from the W-THS, the B-THS shows an extra peak located at 31.5° apart from the anatase TiO$_2$ phase which can be ascribed to carbon (JCPDS No. 46-0943). The carbon in the B-THS is ca. 3.4 wt.% according to the TG data (Figure 4b). Besides, the crystallinity of the B-THS is weaker than that of W-THS. The crystallite size of the B-THS was ca. 19.2 nm calculated by the Scherrer formula, while the B-THS is ca. 11.6 nm. The formed carbon species restrict the growth of nanocrystals in the B-THS. The B-THS shows well-retained hierarchical spherical morphology [Figure 4(c–f)] which is almost the same as the TiO$_2$/HTO precursor. The clear lattice fringes in HRTEM [Figure 4(g)] demonstrate high crystallinity of B-THS, and the interspacing of 0.35 nm matches well with (101) planes of anatase TiO$_2$ (JCPDS No. 21-1272). Besides, due to the presence of residual carbon, as indicated by white circles in Figure 4(g), many lattice defects existed in the B-THS sample. Figure S5 shows SEM and TEM images of the W-THS, the hierarchical spherical structure keeps intact, but the smooth nanosheets structure transformed into a coarse assembly of
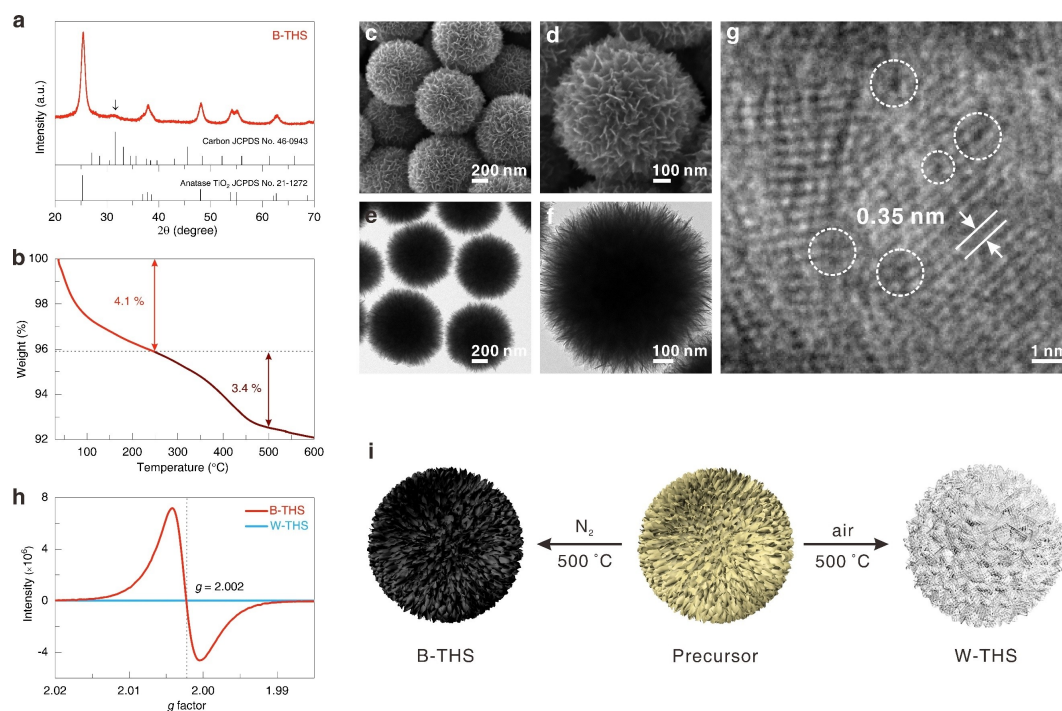

Figure 4. a) XRD, b) TG, c, d) SEM, e, f) TEM and g) HRTEM images of B-THS. h) EPR spectra of B-THS and W-THS. i) Illustration of microstructure evolution from the precursor to B-THS and W-THS by annealing in N$_2$ and air at 500 °C.

large nanoparticles [Figure S5(c,e)]. The BET surface area of B-THS is 115.6 m g^{-1}, while only 44.6 m g^{-1} belongs to the W-THS (Figure S6).

Figure 4(h) shows the EPR spectra of the B-THS and W-THS. The B-THS shows a very strong EPR signal with a g value of 2.002, indicating the existence of abundant oxygen vacancies,[19] while the W-THS sample does not exhibit any EPR response. The O 1s XPS spectra provide auxiliary evidence of the oxygen vacancies (Figure S7). The binding energy centered at 529.8 eV belongs to Ti—O—Ti bonds and the one at 531.3 eV is associated with defect sites with a low oxygen coordination.[7b,20] The peak located at 531.3 eV in the B-THS O1s spectrum shows a much higher integral area proportion (27.8%) than that of W-THS (16.8%), verifying the rich oxygen vacancies character of the B-THS. Figure S8 is the Ti 2p XPS data, no Ti^{3+} signal was detected by XPS. The results agree well with previous reports about V$_O$ or Ti^{3+} doped TiO$_2$.[15a,21] As has been predicted by DFT calculations (Figure 1), the oxygen vacancies in semiconductors will affect the band structure and bandgap which could be directly verified by the optical absorption changes.[22] As shown in Figure S9, in comparison with W-THS, the B-THS displays extended light adsorption from the ultraviolet region to visible light (~750 nm), corresponding to a narrowed bandgap, which as per the color changes shown in Figure S10. The morphology and nanostructure changes from TiO$_2$/HTO precursor to B-THS and W-THS are illustrated in Figure 4i. The dramatic microscopic structural difference be-

tween the B-THS and W-THS shows that the existence of carbon species plays a great role in the growth of TiO$_2$ nanocrystals.

Figure 5(a) shows the galvanostatic charge-discharge profiles of the B-THS and W-THS at 200 mA g^{-1}. The B-THS shows an initial discharge capacity of 282 mAh g^{-1}, and a subsequent charge capacity of 239 mAh g^{-1}, corresponding to an irreversible capacity loss of 15%. This is a lower value than other anatase TiO$_2$ electrodes since the reported initial irreversible capacity loss usually stayed in the 20–40% range.[9] In the second discharge process, the capacity decreased to 252 mAh g^{-1} with a charge capacity of 233 mAh g^{-1}, leading to a much lower capacity loss value of 7.5%. After 50 discharge-charge cycles, a capacity of 210 mAh g^{-1} was still retained [Figure 5(b)]. The discharge capacity of B-THS anode is higher than the reported hydrogenated oxygen-deficient blue anatase (196.1 mAh g^{-1}),[11a] Li$_4$Ti$_5$O$_{12}$-TiO$_2$ hierarchical microspheres (183.5 mAh g^{-1}),[23] and other TiO$_2$ materials (Table S1) with the same operation voltage window. As a control, the W-THS only shows an initial capacity of 151 mAh g^{-1} and remains 138 mAh g^{-1} after 50 cycles [Figure 5(a,c)]. The capacity value is far below that of B-THS. The B-THS possess excellent rate capability at varying discharge-charge current rates ranging from 0.5 to 4 A g^{-1} Figures 5(d) and S11]. The specific capacities for B-THS are 185, 164, 137, and 112 mAh g^{-1} at current rates of 0.5, 1, 2, and 4, respectively, exhibiting superior cycling stability and higher capacity than that of W-THS at each rate. After the high-rate cycling, a stable capacity of 183 mAh g^{-1} can be
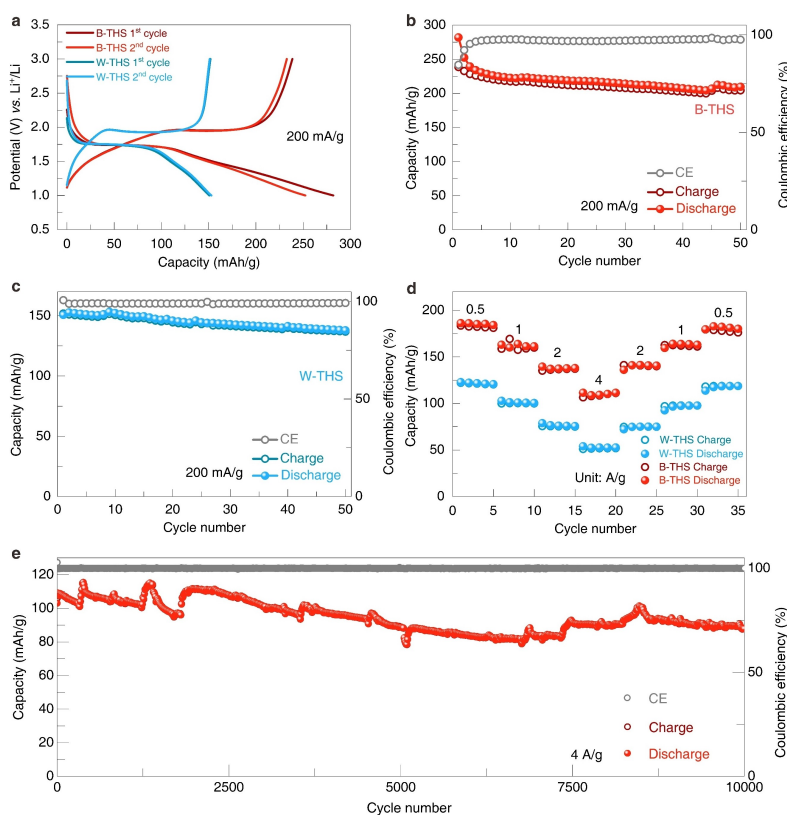

Figure 5. Electrochemical performance of B-THS and W-THS. a) galvanostatic charge-discharge curves, b,c) cycling performance and Coulombic efficiency curves at 200 mA g^{-1}. d) Rate performance of B-THS and W-THS. e) Long-term cycling performance of B-THS at 4 A g^{-1}.

Batteries & Supercaps

Articles
doi.org/10.1002/batt.202100157

Chemistry Europe
European Chemical
Societies Publishing

retained once the current rate is cycled back to $0.2\,A\,g^{-1}$, indicating the robust structural stability of the B-THS. Figures 5e and S12 show the cyclic performance of the B-THS. Remarkably, a discharge capacity of $88\,mAh\,g^{-1}$ (corresponding to a capacity retention of 85.2%) can still be retained after 10000 cycles at $4\,A\,g^{-1}$ by the B-THS. The high-capacity retention achieved by the B-THS validated the structure stability of the as-obtained hierarchical spheres. These results demonstrate the excellent lithium-ion storage capability of the B-THS in terms of long-term cycling stability and good rate performance for the fast charge and discharge. The structure and oxygen vacancies stability of the B-THS after cycling were further validated by the SEM and EPR tests. As shown in Figure S13, the sample keep intact spherical structure. EPR spectrum indicates that the sample shows strong oxygen vacancy signal with g factor at 2.002 (Figure S14).

The above results validate that the as-obtained B-THS hierarchical spheres possess enhanced lithium storage performance in comparison to the W-THS. Specifically, in the oxygen-deficient structure of the B-THS, as validated by DFT, UV-Vis absorption and EIS data (Figure S15), the extra electrons and reduced bandgap will improve the electronic conductivity and charge carrier transport, expediting the electrochemical reaction kinetics of the B-THS. The small primary nanoparticles and permeable porous structure effectively shorten the transport length, favoring the electron transport and Li^+ ions diffusion. The robust, porous hierarchical sphere structure effectively offers plenty of space to accommodate the volume change and prevents the aggregation of nanoparticles, which ensures structural integrity and improves capacity retention upon long-term cycling. These features ensure the oxygen-deficient TiO_2 hierarchical spheres with enhanced lithium storage properties.

3. Conclusions

$TiO_2/H_2Ti_5O_{11}\cdot3H_2O$ hierarchical spheres composed of nanosheets were synthesized by a solvothermal approach. By annealing the precursor in nitrogen, high crystallinity TiO_2 was obtained with well-retained morphology and microscopic structure benefiting from the protection of formed carbon species. The oxygen-deficient environment resulted in the oxygen-deficient TiO_2. EPR and XPS data verified the existence of oxygen vacancies in the B-THS while the UV-Vis spectra showed enhanced visible light absorption, corresponding to the narrowed bandgap. Owing to the rich oxygen vacancies and robust porous hierarchical structure, the oxygen-deficient TiO_2 hierarchical spheres showed superior lithium storage properties, including a high capacity of $282\,mAh\,g^{-1}$ at $200\,mA\,g^{-1}$, enhanced rate capability, and high cyclic stability with a capacity retention of 85.2% over 10000 cycles at $4\,A\,g^{-1}$.

Experimental Section

Calculation methods

The calculations were performed by using the CASTEP plane-wave DFT code[24] with generalized gradient approximation (GGA) functional by Perdew and Wang (PW91).[25] DFT + U method with a value of Ti was set as 7.0 eV (U) under Ref. [26]. A plane-wave basis set with a kinetic energy cutoff of 340 eV was employed in geometric optimization calculations. The sampling k-points were set using the $2\times2\times1$ Monkhorst–Pack meshes for the supercell. The max ionic force, max ionic displacement, and max stress component tolerance were $8.0\times10^{-2}\,eV\,Å^{-1}$, $2.0\times10^{-3}\,Å$, and 0.1 GPa, respectively.

Synthesis of TiO$_2$/HTO (TiO$_2$/H$_2$Ti$_5$O11·3H$_2$O hierarchical spheres)

In a typical procedure, ethylenediamine (EA, Sigma-Aldrich, 0.1 mL) was added to 50 mL of isopropyl alcohol (IPA, Sigma-Aldrich), after vigorously stirring for 10 min, 2 mL of tetra-n-butyl titanate (TBT, Sigma-Aldrich) was added. Continuously stirring for 10 min, the transparent yellowish solution was then transferred to 100 mL of autoclave and kept in an oven at 200 °C for 12 h. After the reaction, the yellowish precipitate was thoroughly washed with ethanol and dried at 80 °C for 24 h.

Synthesis of B-THS (Black TiO$_2$ hierarchical spheres)

The B-THS was synthesized by annealing TiO_2/HTO at 500 °C for 1 h under N_2 with a ramping rate of $2\,°C\,min^{-1}$.

Synthesis of W-THS (White TiO$_2$ hierarchical spheres)

The W-THS was synthesized by annealing TiO_2/HTO at 500 °C for 1 h under air with a ramping rate of $2\,°C\,min^{-1}$.

Material characterization

Crystallographic information of the products was collected on a Rigaku smartLab X-ray diffractometer 9 kW using Cu $K\alpha$ radiation ($\lambda=1.540593$). The morphologies and structures of the samples were characterized by a field-emission scanning electron microscope (FE-SEM, Helios Nanolab 600i, FEI) and transmission electron microscopy (TEM, JEOL, JEM-2100F, 200 kV). TGA/DSC analysis was carried out in an alumina crucible using a TA Instruments SDT Q600 from 30 to 600 °C under a flow of air with a heating rate of 10 °C min^{-1}. The specific surface area and pore size distributions were measured through Brunauer-Emmett-Teller (BET) analysis at 77K on an ASAP 2460, Micromeritics Instrument. X-ray photoelectron spectroscopy (XPS) measurements were taken on a macro mode (3 mm×3 mm, ESCALAB 250, Thermo-VG Scientific) to obtain information about the chemical states of the oxygen element. The electron paramagnetic resonance (EPR) spectra were performed at 2 K on a Bruker EMX plus 10/12 (equipped with Oxford ESR910 Liquid Helium cryostat). The UV-Vis absorbance spectra were conducted on a Japan Shimadzu UV-Vis spectrophotometer (UV-2600) ranging from 300 to 800 nm. FTIR spectrum was recorded on a Thermo IS50R FTIR Spectrum.

Electrochemical measurements

Electrochemical tests were performed using coin cells (2032-type) in the voltage window of 1–3 V using lithium metal as the counter

electrode. The working electrode consisted of 70 wt.% active material (B-THS and W-THS), 20 wt.% conductive agents (carbon black, Super-P), and 10 wt.% polymer binder (poly(vinylidene difluoride), PVDF, Aldrich) was ground into a homogeneous slurry and coated on a stainless-steel mesh, dried at 80 °C in a vacuum oven for 12 h. The electrolyte was a solution of 1 M LiPF6 in a mixture of dimethyl carbonate, ethylene carbonate, and diethyl carbonate (1:1:1 vol%). Polypropylene film (Celgard 2400) was employed as the separator. Cell assembly was conducted in an Ar-filled glovebox with moisture and oxygen concentrations below 0.5 ppm. The galvanostatic discharge/charge was tested on a Neware Battery Testing System (BTS 3000, Shenzhen Neware, China).

Conflict of Interest

The authors declare no conflict of interest.

[1] a) C. F. Liu, C. K. Zhang, H. Y. Fu, X. H. Nan, G. Z. Cao, *Adv. Energy Mater.* **2017**, *7*, 1601127; b) B.-Q. Li, H.-J. Peng, X. Chen, S.-Y. Zhang, J. Xie, C.-X. Zhao, Q. Zhang, *CCS Chem.* **2019**, *1*, 128; c) W. Zhang, H. Xia, Z. Zhu, Z. Lv, S. Cao, J. Wei, Y. Luo, Y. Xiao, L. Liu, X. Chen, *CCS. Chem.* **2020**, *2*, 1245; d) Y. Wu, X. Huang, L. Huang, J. Chen, *Energy Environ. Mater.* **2021**, *4*, 19; e) J. B. Goodenough, H. Gao, *Sci. China Chem.* **2019**, *62*, 1555; f) Z. Zeng, X. Liu, X. Jiang, Z. Liu, Z. Peng, X. Feng, W. Chen, D. Xia, X. Ai, H. Yang, Y. Cao, *InfoMat* **2020**, *2*, 984; g) C. Zu, H. Yu, H. Li, *InfoMat* **2021**, *3*, 648; h) K. Sun, Z. Peng, InfoMat, DOI: https://doi.org/10.1002/inf2.12216.

[2] a) H. Ren, R. B. Yu, J. Y. Wang, Q. Jin, M. Yang, D. Mao, D. Kisailus, H. J. Zhao, D. Wang, *Nano Lett.* **2014**, *14*, 6679; b) W. Li, F. Wang, S. S. Feng, J. X. Wang, Z. K. Sun, B. Li, Y. H. Li, J. P. Yang, A. A. Elzatahry, Y. Y. Xia, D. Y. Zhao, *J. Am. Chem. Soc.* **2013**, *135*, 18300; c) X. Xiao, L. Zou, H. Pang, Q. Xu, *Chem. Soc. Rev.* **2020**, *49*, 301; d) X. Liu, L. Zhao, S. Wang, M. Chao, Y. Li, J. Leng, J. Zhang, Z. Tang, *Sci. Bull.* **2019**, *64*, 1148.

[3] a) B. J. Morgan, G. W. Watson, *Phys. Rev. B* **2010**, *82*, 144119; b) J. Ye, W. Liu, J. Cai, S. Chen, X. Zhao, H. Zhou, L. Qi, *J. Am. Chem. Soc.* **2011**, *133*, 933.

[4] a) J.-Y. Shin, D. Samuelis, J. Maier, *Adv. Funct. Mater.* **2011**, *21*, 3464; b) J. S. Chen, Y. L. Tan, C. M. Li, Y. L. Cheah, D. Luan, S. Madhavi, F. Y. C. Boey, L. A. Archer, X. W. Lou, *J. Am. Chem. Soc.* **2010**, *132*, 6124.

[5] X. Gao, G. Li, Y. Xu, Z. Hong, C. Liang, Z. Lin, *Angew. Chem. Int. Ed.* **2015**, *54*, 14331.

[6] a) L. Ma, X. Gao, W. Zhang, H. Yuan, Y. Hu, G. Zhu, R. Chen, T. Chen, Z. Tie, J. Liu, T. Wu, Z. Jin, *Nano Energy* **2018**, *53*, 91; b) Y. Zhang, Z. Ding, C. W. Foster, C. E. Banks, X. Qiu, X. Ji, *Adv. Funct. Mater.* **2017**, *27*, 1700856; c) H. Zhang, J. Wang, Q. Liu, W. He, Z. Lai, X. Zhang, M. Yu, Y. Tong, X. Lu, *Energy Storage Mater.* **2019**, *21*, 154; d) Z. Li, Y. Ren, L. Mo, C. Liu, K. Hsu, Y. Ding, X. Zhang, X. Li, L. Hu, D. Ji, G. Cao, *ACS Nano* **2020**, *14*, 5581.

[7] a) J. Kang, J. Kim, S. Lee, S. Wi, C. Kim, S. Hyun, S. Nam, Y. Park, B. Park, *Adv. Energy Mater.* **2017**, *7*, 1700814; b) Y. Wu, Y. Jiang, J. Shi, L. Gu, Y. Yu, *Small* **2017**, *13*, 1700129; c) Q. Ni, R. Dong, Y. Bai, Z. Wang, H. Ren, S. Sean, F. Wu, H. Xu, C. Wu, *Energy Storage Mater.* **2020**, *25*, 903.

[8] a) U. Lafont, D. Carta, G. Mountjoy, A. V. Chadwick, E. M. Kelder, *J. Phys. Chem. C* **2010**, *114*, 1372; b) K. Shen, H. Chen, F. Klaver, F. M. Mulder, M. Wagemaker, *Chem. Mater.* **2014**, *26*, 1608.

[9] a) D.-H. Lee, B.-H. Lee, A. K. Sinha, J.-H. Park, M.-S. Kim, J. Park, H. Shin, K.-S. Lee, Y.-E. Sung, T. Hyeon, *J. Am. Chem. Soc.* **2018**, *140*, 16676; b) G. Zhang, H. B. Wu, T. Song, U. Paik, X. W. Lou, *Angew. Chem. Int. Ed.* **2014**, *53*, 12590.

[10] a) W.-Q. Wu, Y.-F. Xu, J.-F. Liao, L. Wang, D.-B. Kuang, *Nano Energy* **2019**, *62*, 791; b) Z. Zhang, P. Xu, H. Zhang, A. Shen, Y. Zhao, *ACS Appl. Mater. Interfaces* **2019**, *2*, 5744; c) F. Xiong, F. Lv, C. Tang, P. Zhang, S. Tan, Q. An, S. Guo, L. Mai, *Sci. China Mater.* **2020**, *63*, 1993.

[11] a) J. Zheng, Y. Liu, G. Ji, P. Zhang, X. Cao, B. Wang, C. Zhang, X. Zhou, Y. Zhu, D. Shi, *ACS Appl. Mater. Interfaces* **2015**, *7*, 23431; b) Z. Hao, Q. Chen, W. Dai, Y. Ren, Y. Zhou, J. Yang, S. Xie, Y. Shen, J. Wu, W. Chen, G. Q. Xu, *Adv. Energy Mater.* **2020**, *10*, 1903107.

[12] a) Y. Cai, H. E. Wang, X. Zhao, F. Huang, C. Wang, Z. Deng, Y. Li, G. Z. Cao, B. L. Su, *ACS Appl. Mater. Interfaces* **2017**, *9*, 10652; b) H. Liu, Z. Bi, X.-G. Sun, R. R. Unocic, M. P. Paranthaman, S. Dai, G. M. Brown, *Adv. Mater.* **2011**, *23*, 3450.

[13] L. Ngamwongwan, I. Fongkaew, S. Jungthawan, P. Hirunsit, S. Limpijumnong, S. Suthirakun, *Phys. Chem. Chem. Phys.* **2021**, *23*, 11374.

[14] a) T. Sasaki, K. M. Yu, Y. Fujiki, *Chem. Mater.* **1992**, *4*, 894; b) H. G. Yang, H. C. Zeng, *J. Am. Chem. Soc.* **2005**, *127*, 270.

[15] a) Y. Zhang, C. W. Wang, H. S. Hou, G. Q. Zou, X. B. Ji, *Adv. Energy Mater.* **2017**, *7*, 1600173; b) Z.-Q. Li, W.-C. Chen, F.-L. Guo, L.-E. Mo, L.-H. Hu, S.-Y. Dai, *Sci. Rep.* **2015**, *5*, 14178.

[16] Q. Chen, B. Ren, Y. Zhao, X. Xu, H. Ge, R. Guan, J. Zhao, *Chem. Eur. J.* **2014**, *20*, 17039.

[17] a) L. E. Mo, Z. Q. Li, Y. C. Ding, C. Gao, L. H. Hu, Y. Huang, T. Hayat, A. Alsaedi, S. Y. Dai, *Sol. Energy* **2019**, *177*, 448; b) H. Li, Z. Bian, J. Zhu, D. Zhang, G. Li, Y. Huo, H. Li, Y. Lu, *J. Am. Chem. Soc.* **2007**, *129*, 8406.

[18] H. B. Wu, X. W. Lou, H. H. Hng, *Chem. Eur. J.* **2012**, *18*, 2094.

[19] a) C. Zhao, Y. Cai, K. Yin, H. Li, D. Shen, N. Qin, Z. Lu, C. Liu, H.-E. Wang, *Chem. Eng. J.* **2018**, *350*, 201; b) J. Chen, Z. Ding, C. Wang, H. Hou, Y. Zhang, C. Wang, G. Zou, X. Ji, *ACS Appl. Mater. Interfaces* **2016**, *8*, 9142.

[20] Y. Xu, M. Zhou, X. Wang, C. Wang, L. Liang, F. Grote, M. Wu, Y. Mi, Y. Lei, *Angew. Chem. Int. Ed.* **2015**, *54*, 8768.

[21] a) G. Liu, L.-C. Yin, J. Wang, P. Niu, C. Zhen, Y. Xie, H.-M. Cheng, *Energy Environ. Sci.* **2012**, *5*, 9603; b) Y. Yang, G. Liu, J. T. S. Irvine, H.-M. Cheng, *Adv. Mater.* **2016**, *28*, 5850.

[22] a) H. C. Wang, C. Y. Fan, Y. P. Zheng, X. H. Zhang, W. H. Li, S. Y. Liu, H. Z. Sun, J. P. Zhang, L. N. Sun, X. L. Wu, *Chem. Eur. J.* **2017**, *23*, 9666; b) Y. Q. Yang, L. C. Yin, Y. Gong, P. Niu, J. Q. Wang, L. Gu, X. Q. Chen, G. Liu, L. Z. Wang, H. M. Cheng, *Adv. Mater.* **2018**, *30*, 1704479.

[23] D. Li, W. Zhao, L. Cao, Y. Y. Gao, Y. H. Liu, W. J. Wang, T. Qi, *ChemSusChem* **2019**, *12*, 4461.

[24] a) J. P. Perdew, A. Ruzsinszky, G. I. Csonka, O. A. Vydrov, G. E. Scuseria, L. A. Constantin, X. Zhou, K. Burke, *Phys. Rev. Lett.* **2008**, *100*, 136406; b) V. Milman, B. Winkler, J. A. White, C. J. Pickard, M. C. Payne, E. V. Akhmatskaya, R. H. Nobes, *Int. J. Quantum Chem.* **2000**, *77*, 895.

[25] J. P. Perdew, Y. Wang, *Phys. Rev. B* **1992**, *45*, 13244.

[26] C. Zhao, D. Huang, J. Chen, Y. Li, Z. Du, *RSC Adv.* **2016**, *6*, 98908.